

Probing disorder-driven topological phase transitions via topological edge modes with ultracold atoms in Floquet-engineered honeycomb lattices

Alexander Hesse, Johannes Arceri, Moritz Hornung, Christoph Braun, Monika Aidelsburger*

Max-Planck-Institut für Quantenoptik, 85748 Garching, Germany

Munich Center for Quantum Science and Technology (MCQST), 80799 München, Germany

Fakultät für Physik, Ludwig-Maximilians-Universität, 80799 München, Germany

(Dated: August 29, 2025)

One of the most fascinating properties of topological phases of matter is their robustness to disorder and imperfections. Although several experimental techniques have been developed to probe the geometric properties of engineered topological Bloch bands with cold atoms, they almost exclusively rely on the translational invariance of the underlying lattice. This prevents direct studies of topology in the presence of disorder, further hindering an extension to disordered interacting topological phases. Here, we identify disorder-driven phase transitions between two distinct Floquet topological phases using the characteristic properties of topological edge modes with ultracold atoms in periodically-driven two-dimensional (2D) optical lattices. Our results constitute an important step towards studying the rich interplay between topology and disorder with cold atoms. Moreover, our measurements confirm that disorder indeed favors the anomalous Floquet topological regime over conventional Hall systems, indicating an enhanced robustness and paving the way towards observing exotic out-of-equilibrium phases such as the anomalous Floquet Anderson insulator.

The discovery of topological phases of matter has revolutionized condensed matter physics [1, 2]. Remarkably, disorder plays a crucial role in revealing topological robustness. A prominent example is the quantization of Hall plateaus in the integer [3] and fractional quantum Hall effects [4]. While strong disorder eventually induces a transition to a trivial regime when its amplitude approaches the spectral gap, weak disorder is essential for pinning the Fermi energy within the gap, thereby stabilizing the plateaus with extraordinary precision.

Synthetic quantum systems offer unique opportunities to study the properties and exotic excitations of topological phases of matter [5, 6] with microscopic resolution and control [7]. With neutral atoms in optical lattices, topological phases are typically engineered via periodic driving (Floquet engineering) [8–10], or synthetic dimensions [11–14]. This has enabled the realization of Hofstadter [12, 13, 15–17] and Haldane-type models [18–20], with recent advances in studying strongly-interacting regimes [21–23]. Moreover, numerous techniques have been developed to characterize the engineered geometric properties of Floquet-Bloch bands [6] with high precision [18, 19, 24–29]. While this provides an excellent starting point for studying the rich interplay between topology and disorder [30–33], experimental studies remain scarce.

Topological pumps [34] – 1D dynamical versions of 2D topological systems – offer a simpler experimental and theoretical route for investigating topology and disorder [35]. Indeed, disorder-induced phase transitions have been studied in the context of 1D topological Thouless pumps in photonic waveguide arrays [36], with neutral atoms [37], superconducting qubits [38] and in metamaterials [39]. Disorder can further drive a transition

from a topologically trivial to a non-trivial phase known as topological Anderson insulators and has been studied experimentally in 1D topological pumps [37] and 1D momentum-space lattices [40], while 2D realizations have so far only been reported in photonic systems [41–43].

Chiral edge modes serve as clear signatures of phase transitions between topologically trivial and non-trivial regimes [44, 45]. In this work, we extend this idea by demonstrating that mode matching between a localized Bose-Einstein condensate (BEC) – precisely controlled via an optical tweezer [29] – and topologically protected chiral edge modes can be exploited to selectively prepare edge modes in distinct Floquet topological regimes. This enables the study of topological phase transitions in the presence of disorder, which we introduce using an optical speckle potential [46, 47]. Specifically, we investigate disorder-driven transitions between the anomalous Floquet (AF) and Haldane (H) topological regimes in a 2D periodically-modulated honeycomb lattice (Fig. 1a). Our experimental observations are in agreement with numerical simulations, underscoring the reliability of our approach. Central to this is a newly developed method for calibrating the average disorder strength, based on Kapitza-Dirac diffraction of a BEC [48]. In contrast, earlier methods relied on optical calibrations in a conjugate imaging plane [49] or state-dependent disorder potentials [50, 51] limiting their applicability to more general settings.

The technique builds on our recent work on the observation of topological chiral edge modes [29]: A localized BEC is confined in a tightly-focused optical tweezer trap near a topological interface generated via a programmable repulsive potential step (Fig. 1b). After release, the in-situ evolution of the atoms reveals the presence or absence of chiral motion. Distinct Floquet topological phases are realized via chiral modulation of the three tunnel couplings (Fig. 1a), as demonstrated in

* monika.aidelsburger@mpq.mpg.de

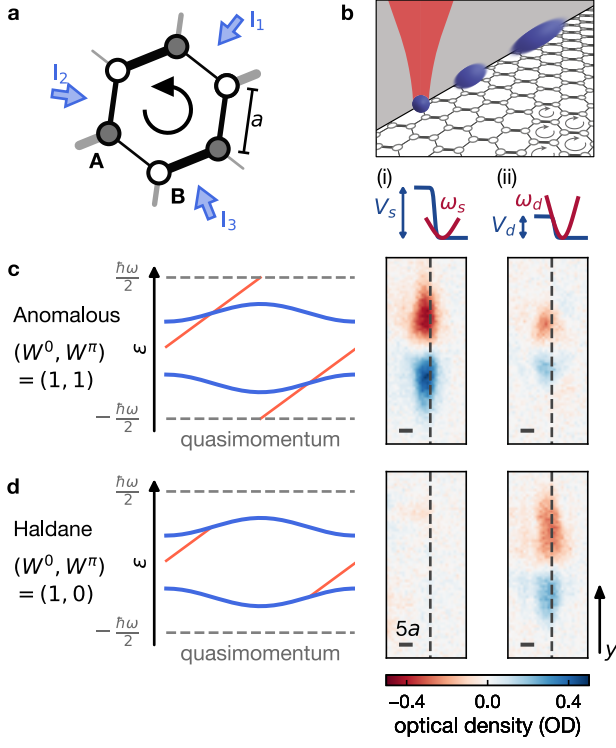


Figure 1. Experimental setup and measurement protocol. **a** Schematic of the periodically-modulated honeycomb lattice generated by interfering three laser beams with variable intensities $I_i(t)$, $i = \{1, 2, 3\}$ and $a = 287$ nm. The width of the tunneling bonds indicates their variable strength, modulated in a chiral manner with frequency ω . **b** Schematic of the preparation of edge modes at a topological interface: A tightly-focused optical tweezer (red) confines a BEC (blue), which is prepared and released at a repulsive potential step (gray). Bottom: Two different experimental settings to tune the initial-state: (i) Shallow tweezer with radial harmonic oscillator frequency $\omega_s/(2\pi) = 1.3(1)$ kHz and large potential step $V_s/h = 13.2$ kHz. (ii) Deep tweezer with radial frequency $\omega_d/(2\pi) = 2.0(1)$ kHz and potential height $V_d/h = 2.8$ kHz. **c, d** Left: Winding numbers (W^0, W^π) and schematic band-structure (blue) of the **c** anomalous Floquet $[\omega/(2\pi) = 7$ kHz] and **d** Haldane $[\omega/(2\pi) = 16$ kHz] regime. Edge dispersion is marked in red. Right: Difference of absorption pictures (averaged over 100 images per chirality) obtained for the two different chiralities $\kappa = \pm 1$ after $50T$, with $T = 2\pi/\omega$, for the two experimental settings (i, ii) illustrated at the top. The dashed vertical line indicates the location of the topological interface.

Ref. [20]. Floquet topological phases are characterized by so-called winding numbers, which determine the number and chirality of topological edge modes in a specific quasienergy gap. For a generic two-band model there are two different energy gaps, one around zero energy (0-gap) and one at the Floquet Brillouin zone edge (π -gap) with winding numbers (W^0, W^π) . The generalized bulk-boundary correspondence connects the Chern number of each band to the winding number according to:

$C^\mp = \pm(W^0 - W^\pi)$ [52–54], where C^- (C^+) denotes the Chern number of the lower (upper) band. Here, we focus on two distinct topological regimes: the anomalous Floquet (Fig. 1c) with $(W^0, W^\pi) = (1, 1)$ and the Haldane regime (Fig. 1d) with $(1, 0)$, both supporting topological edge modes with the same chirality.

The overlap between the BEC and the edge mode can be tuned by changing the strength of the harmonic confinement of the tweezer allowing us to distinguish the two regimes with high precision [29, 48]. Here, we make use of the unique property of anomalous Floquet topological systems which support an edge mode at each quasienergy ϵ , making it extremely robust to the initial-state parameters of the wave packet (Fig. 1c). In contrast, the observation of edge modes in the Haldane regime (0-gap) sensitively depends on the initial state (Fig. 1d) since it is located at non-zero quasimomentum (K and K' points). By adjusting the tweezer depth we find that a shallow confinement ω_s suppresses the overlap with the edge mode in the Haldane regime, while maintaining a large overlap with the edge mode in the π -gap in the anomalous regime. Intuitively, this can be understood by looking at the spatial wavefunction of the edge mode in both regimes. A shallow tweezer generates a BEC at zero quasimomentum, which has good overlap with the π -gap edge mode in the anomalous regime, but essentially no overlap with the 0-gap edge mode at finite quasimomentum. In order to further enhance the differential signal we choose a large potential step V_s for generating the interface in the anomalous regime, as it increases the edge-mode velocity, while a shallow potential step V_d is beneficial for large edge-mode velocities in the Haldane regime due to the smaller characteristic energy gap (Fig. 1c, d). For experiments where we study edge-mode propagation in the Haldane regime, we find that a larger radial confinement ω_d results in good overlap with the 0-gap edge mode in both regimes.

The experimental sequence starts by generating a BEC of ^{39}K atoms in a crossed optical dipole trap. By adding a tightly-focused optical tweezer trap at $\lambda_T = 1064$ nm a tightly-localized BEC of about 200 atoms is formed, whose position is controlled using a 2D acousto-optical deflector (AOD) that allows us to precisely align the position of the BEC relative to the topological interface. Residual atoms not loaded into the tweezer trap are expelled by lowering the large-volume crossed optical dipole trap. While holding the atoms in the tweezer trap, a programmable repulsive optical potential realizing the topological interface is ramped up. The potential is generated using a digital micromirror device (DMD), which is illuminated by a spatially and spectrally incoherent light source with a wavelength centered around $\lambda_S = 638$ nm [29]. Subsequently, a hexagonal optical lattice, generated by three free-running laser beams ($\lambda_L = 745$ nm), interfering under an angle of 120° , is ramped up to a depth of $5.9E_R$ (Fig. 1a), where $E_R/h = h/(2\lambda_L^2 m_K) = 9.23$ kHz is the recoil energy, h Planck’s constant and m_K the mass of ^{39}K . The

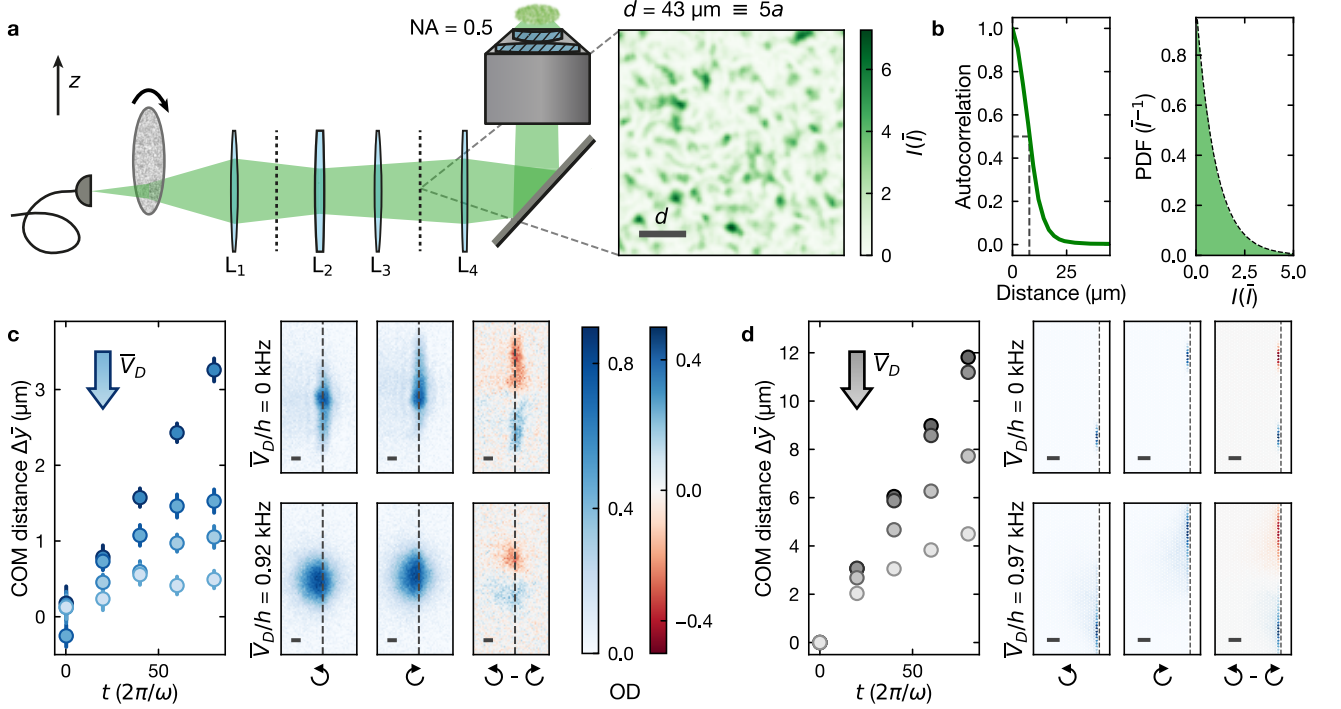


Figure 2. **Optical speckle potential and disorder-induced renormalization of edge-mode propagation in the Haldane regime.** **a** Schematic drawing of the optical speckle setup. The uncollimated output of a photonic-crystal-fiber illuminates a small area on a diffuser, scrambling the phase profile of the laser beam. This results in a speckle pattern in the Fourier plane of a lens, which is imaged onto the atoms using two telescopes with a total demagnification of 45. Planes conjugate to the atomic plane are marked by dashed lines. Inset: Measured exemplary optical speckle pattern. **b** Left: Radially averaged autocorrelation function with half width half maximum $7.9\mu\text{m}$ (dashed lines) evaluated from speckle patterns, as shown in **a**. We expect the correlation length in the atomic plane to be on the order of $\sigma_r = 0.3\mu\text{m}$. Right: Expected probability density function (PDF) of a speckle pattern (dashed line) together with a histogram of the speckle intensity evaluated from 118 individual images ($720\mu\text{m} \times 720\mu\text{m}$) before demagnification. **c** Experimental data (deep tweezer parameters: ω_d , V_d) and **d** numerical simulation for the edge state propagation in the Haldane regime for $\bar{V}_D/h = [0\text{ kHz}, 0.46\text{ kHz}, 0.92\text{ kHz}, 1.39\text{ kHz}]$ and $\omega/(2\pi) = 16\text{ kHz}$. The disorder strength is encoded in the color of the data points. For the experimental results, each data point is averaged over 39-40 disorder realizations, for the numerical data we average over 100 disorder realizations. Error bars are extracted via bootstrapping. Right: In-situ pictures after $80T$ for both chiralities (indicated by the arrows) as well as their difference for two disorder strengths $\bar{V}_D/h = [0\text{ kHz}, 0.92\text{ kHz}]$. The vertical dashed line indicates the location of the topological interface. All scale bars have length $5a$. For the numerical results, the lattice site population is normalized to have a peak value of 1.

periodic modulation is realized by varying the intensities of the three laser beams out of phase according to $I_i(t) = I_0(1 - m + m \cos(\omega t + \phi_i))$, with ω the modulation frequency, m the modulation amplitude, $\phi_i = \kappa \frac{2\pi}{3} i$ the phase for the i th lattice beam ($i = \{1, 2, 3\}$), and $\kappa = \pm 1$ the chirality of the modulation. After turning on the lattice, the modulation is linearly ramped to its final value $m = 0.25$ within $5T$, where T is one modulation cycle. At the end of the ramp, the atoms are suddenly released from the tweezer trap and we monitor the in-situ time evolution of the cloud after a variable time t . The vertical overlap of the tweezer focus and dipole trap is optimized for each experimental run to avoid excitations perpendicular to the 2D lattice, which, together with the dipole trap, has a combined trap frequency $\omega_z/(2\pi) = 0.33(3)\text{ kHz}$, and interaction effects are

suppressed by setting the scattering length to $6a_0$, where a_0 is the Bohr radius.

To introduce controlled disorder, we generate a repulsive optical speckle potential at a wavelength of 532 nm . Optical speckle potentials are well-established tools in quantum simulation experiments [47, 55], particularly in studies of Anderson localization [46, 56–60], offering disorder with well-characterized statistics and tunable strength over several orders of magnitude. In our setup, a lens transforms a random phase pattern, generated by a holographic diffuser, into a speckle field in the Fourier plane of the lens. This pattern is then projected into the atomic plane using a high-resolution imaging objective with $\text{NA} = 0.5$ (Fig. 2a). Assuming diffraction-limited performance of the objective, we estimate a speckle correlation length of $\sigma_r = 0.3\mu\text{m}$ in the horizontal plane

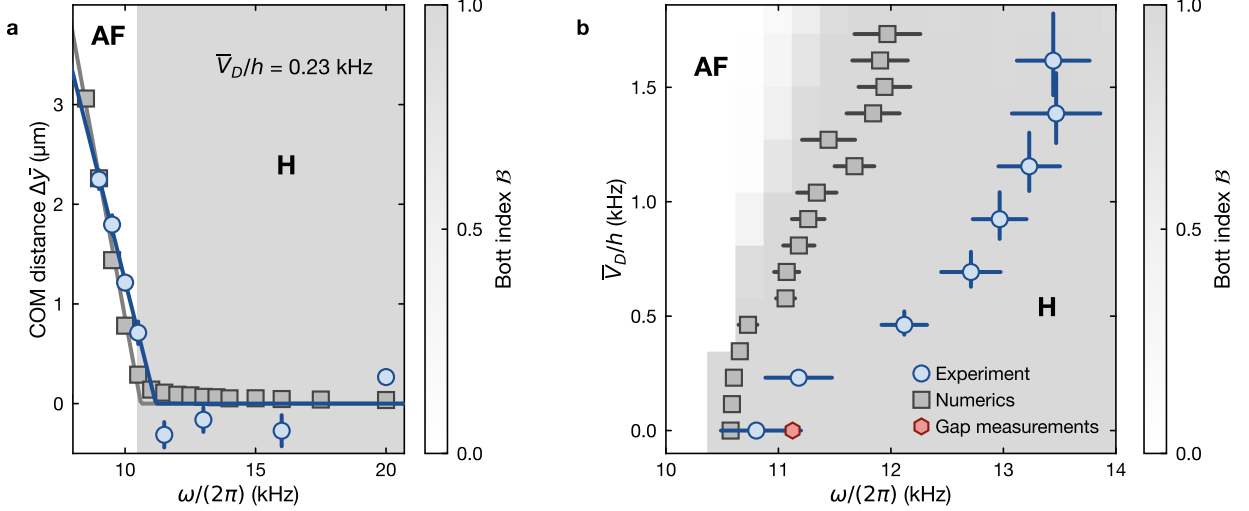


Figure 3. **Measurement of the disorder-driven shift of the topological phase transition.** **a** COM distance $\Delta\bar{y}$ as a function of modulation frequency. The solid lines are fits of the function $\max(-\eta_1 \omega + \eta_0, 0)$ (η_1 and η_0 are free fit parameters) to extract the phase transition point for the experimental (blue) and numerical data (gray). The latter has been simulated based on a simplified two-band model for $20T$ and was averaged over 100 disorder realizations. Error bars for experiment and numerics are extracted via bootstrapping. Each experimental data point is the average of 19-20 measurements per chirality, taken for different disorder realizations and after $50T$. The grey shading in the background encodes the Bott index \mathcal{B} , evaluated for 100 (200) disorder realizations for $\bar{V}_D/h < 1$ kHz ($\bar{V}_D/h \geq 1$ kHz) on $N_s = 576$ lattice sites. The labels (AF) and (H) indicate the anomalous ($\mathcal{B} = 0$) and Haldane regime ($\mathcal{B} = 1$) respectively. **b** Shift of the topological phase transition obtained from measurements (blue) and numerical simulations (gray) extracted from fits as shown in **a**. The horizontal error bars show the error of the fit illustrated in **a**. The vertical error bar reflects the calibration error of the disorder strength [48]. The red data point indicates a gap-closing measurement for $\bar{V}_D = 0$ and determines the phase transition for the bandstructure realized in the experiment (see main text).

and $\sigma_z \simeq 2.4 \mu\text{m}$ in the vertical direction, much larger than the harmonic oscillator length in the z -direction. The intensity distribution of the resulting disorder potential closely follows the expected probability density function $p_I(I) = \bar{I}^{-1} \exp[-I/\bar{I}]$, with \bar{I} being the average intensity [47]. Its strength has been calibrated using diffraction measurements [48], providing the proportionality constant α_I for the potential energy shift seen by the atoms, $\bar{V}_D = \alpha_I \bar{I}$. In the optical setup we further displace the diffuser from the optical axis, such that rotating it results in different potential disorder realizations with similar statistics, as different patches on the diffuser will be illuminated. We use this to average over different disorder realizations.

We start by investigating the propagation of chiral edge modes in the presence of disorder. For weak disorder, it is expected that disorder induces couplings between different quasimomenta within the edge-mode dispersion, resulting in a renormalization of the edge-mode velocity. This is of particular relevance in the context of topological photonics [61, 62], where disorder and imperfections can hinder practical applications. We focus on the Haldane regime, where the system hosts a single chiral edge mode within the 0-gap. The modulation parameters are chosen to lie well within the topological phase, sufficiently far from any phase transition. To

probe the effect of disorder, we measure the difference in the center-of-mass (COM) position $\Delta\bar{y} = \bar{y}_{+1} - \bar{y}_{-1}$ of the wavepacket for both chiralities along the topological interface (aligned along the y -direction) at various evolution times, where \bar{y}_κ denotes the COM position evaluated from in-situ absorption images, as shown in Fig. 2c,d. The in-situ images further reveal that disorder not only slows down edge transport but also induces propagation into the bulk. This is further reflected in a reduced overall transport velocity, evident from the shorter COM distance traveled by the atoms. The velocity observed in the experiment is further suppressed compared to numerical simulations. We attribute this to the finite width of the topological interface and the more finely tuned overlap with the initial state used in the numerics [29, 63–65]. We find qualitatively similar behavior in the anomalous regime.

To study the disorder induced shift of the transition between the Haldane and Anomalous Floquet regimes we utilize the preparation scheme introduced in Fig. 1c,d. While the specifics of edge-mode propagation depend on the disorder potential, the presence or absence of chiral motion at the topological interface provides a robust observable for distinguishing between topological regimes. To enhance the contrast between the anomalous Floquet and the Haldane regime, we choose a large potential step

V_s in combination with a shallow tweezer ω_s and measure the COM displacement between the two chiralities after a fixed evolution time, as a function of modulation frequency (Fig. 3a). In the anomalous regime at lower modulation frequencies, we observe clear chiral motion, which gradually diminishes near the topological phase transition. Beyond a critical frequency, the signal vanishes, marking the transition to the Haldane regime. This behavior is in agreement with numerical simulations. We determine the critical point by fitting a kink function to the experimental and numerical data. Note that the absolute value of the COM distances differs between the numerical simulations and the experiment, as described above. The robustness of this method for identifying the phase transition is further validated by benchmarking against calculations of the Bott index \mathcal{B} [66, 67] – a topological invariant equivalent to the Chern number that is particularly suited to study disordered systems. Here, we compute the Bott index for the lowest band of a simplified two-band model, as described in detail in Ref. [48]. We identify the region in the phase diagram with a disorder-averaged Bott index $\mathcal{B} = 1$ with the Haldane regime, where $\mathcal{C}^\mp = \pm 1$ and the region with $\mathcal{B} = 0$ with the anomalous regime, where $\mathcal{C}^\mp = 0$.

We further benchmark our method without disorder ($\bar{V}_D = 0$) via comparison to standard gap-closing measurements based on Stückelberg interferometry (red data point in Fig. 3b) [20, 68, 69]. This measurement determines the location of the phase transition at 11.13(8) kHz. The systematic shift between this gap-closing measurement and the numerical simulations based on a simple two-band model (Bott index in Fig. 3b) is due to mixing with higher bands in the experiment. Extending the simulations to a 6-band model, we identify the phase transition at 10.92 kHz in agreement with the experimental results. Tracking the phase transition as a function of the applied disorder potential, we observe that the transition shifts to higher modulation frequencies with increasing disorder (Fig. 3b), suggesting that disorder favors the anomalous Floquet topological regime, in agreement with theoretical predictions [32]. We attribute the systematic shift between the experiment and theory to the role of higher bands. Numerical studies further suggest that the observed transition shift is quite generic, with only a weak dependence on the correlation length of the disorder potential.

Anomalous Floquet systems are predicted to exhibit a rich phase diagram at large disorder strengths (schematic phase diagram: Fig. 4a). In particular, the interplay between periodic driving and disorder can stabilize genuine out-of-equilibrium topological phases known as the Anomalous Floquet Anderson insulator (AFAI) [31, 33, 70], where a fully localized bulk coexists with an extended topological edge mode. More generally, one expects a transition to the topologically trivial regime once disorder strengths become comparable to the bulk energy gap. Experimentally, this trivial phase is characterized by the disappearance of chiral motion, independent of

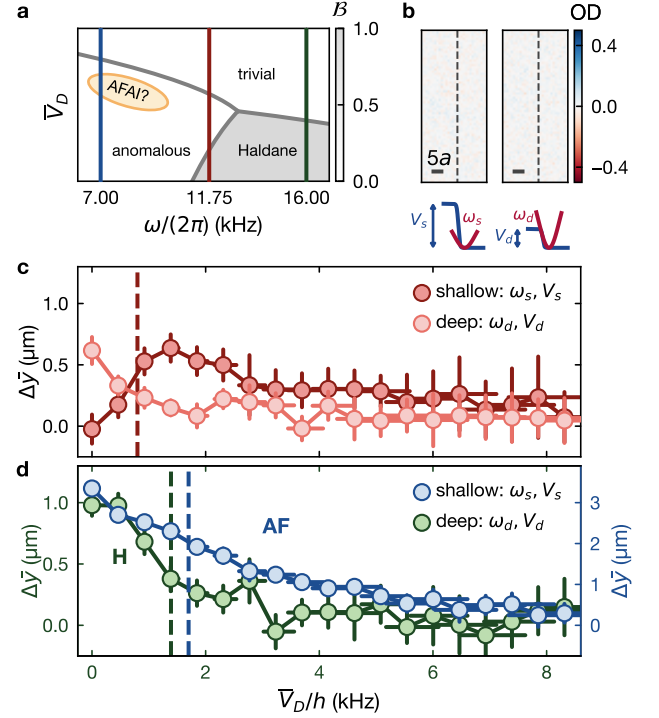


Figure 4. Topological phase diagram for large potential disorder. **a** Schematic phase diagram illustrating three different phases: anomalous Floquet, Haldane and topologically trivial. The orange ellipse indicates the potential region of an AFAI phase. The dashed lines indicate the parameter regime for the experimental data shown in **c,d**. **b** Difference of absorption pictures obtained for the two different chiralities $\kappa = \pm 1$ (averaged over 100 disorder realizations) after $50T$ at $\bar{V}_D/h = 11.1$ kHz for the two experimental settings illustrated below. **c,d** COM distance after $50T$ for variable disorder strength and different modulation parameters. The dashed vertical lines indicate the corresponding minimal energy gap without disorder obtained from a 6-band calculation. **c** Re-entrance behavior of the edge mode signal for two different experimental settings optimized for the anomalous (dark red) and Haldane (light red) regime, respectively. The modulation frequency $[\omega/(2\pi) = 11.75$ kHz] is chosen to lie close to the phase transition at zero disorder. **d** Transition to the topologically-trivial regime deep in the anomalous [blue, $\omega/(2\pi) = 7$ kHz] and Haldane regime [green, $\omega/(2\pi) = 16$ kHz]. Error bars on $\Delta\bar{y}$ have been extracted by bootstrapping. The error bars in \bar{V}_D give the calibration error of the disorder strength. The blue trace has been plotted on a separate axis on the right due to the much larger COM distance traversed. Each data point is the average of 19-20 measurements per chirality, with different disorder patterns applied.

the initial-state parameters of the BEC (Fig. 4b). To probe this phase diagram, we monitor the chiral signal while varying the disorder strength at fixed modulation parameters. Cuts through the phase diagram are illustrated in Fig. 4a. Starting near the phase transition in

the Haldane regime we find a re-entrant behavior of chiral motion, signaling a transition from the Haldane to the anomalous regime at weak disorder (Fig. 4c). For large disorder the chiral signal gradually disappears, which we interpret as a transition to the topologically-trivial phase. This dataset was taken with the optimal parameters for the anomalous regime (V_s, ω_s). Taking the same scan for a deep tweezer ω_d and shallow potential step V_d , we find a weak signal in the Haldane regime at low modulation frequencies as expected. The signal gradually disappears for larger modulation frequencies, further supporting that at large disorder the system enters the trivial phase.

In a second set of measurements, we study the behavior deep in the anomalous and Haldane regime where the experimental parameters have been chosen to maximize the signal in each respective regime (Fig. 4d). We find that in both cases the chiral signal gradually vanishes and it appears that the transition to the trivial regime happens already at much lower values for the Haldane compared to the anomalous regime despite the fact that the minimal energy gap in the Floquet spectrum is comparable (dashed vertical lines in Fig. 4d). Previous work indicates that the relevant energy scale in the anomalous regime is rather determined by the width of the Floquet Brillouin zone, i.e., $\omega/(2\pi) = 7$ kHz, which is much larger than the minimal gap. Note that the vertical scale is different for both data sets for better visibility. This observation further supports theoretical work suggesting an enhanced robustness of anomalous Floquet topological insulators (AFTIs) compared to conventional Chern insulators.

In conclusion, edge modes provide a powerful probe for exploring topological phase transitions. While energy-selective excitation of edge and bulk modes is relatively straightforward in photonic systems [61, 62], no practical counterpart exists for neutral atoms in optical lattices. In this work, we demonstrate a novel method for selectively preparing chiral edge modes by tailoring the properties of the initial wavepacket to enhance the overlap with the localized mode at the interface. We have benchmarked the robustness of this approach through numerical simulations and comparisons with the Bott index. We further presented the first experimental investigation of disorder-driven phase transitions between two distinct topological phases in synthetic quantum systems, which are inaccessible using conventional observables [6]. In the future, these concepts could be extended through energy-resolved preparation schemes, where a cold reservoir is coupled to an initially empty lattice and the injection energy is tuned via the relative chemical potential [71].

When combined with microscopic control over initial-state preparation [7, 72], this opens exciting new avenues for studying the dynamics and robustness of topological edge modes, with particular relevance for applications in topological photonics [61, 62].

Exploring topological phases of matter in the presence of disorder further opens new avenues for investigating exotic Floquet topological phases. AFTIs share key features with conventional Chern insulators, such as quantized chiral edge states. However, AFTIs also support novel phases, where all bulk states are localized coexisting with extended edge modes, so-called AFAIs [31, 33, 70]. This unique behavior arises from the protection of topological properties by Floquet symmetry, making AFTIs intrinsically more robust than conventional Chern insulators. AFAIs exhibit remarkable resilience to temporal noise [73, 74], and initial theoretical work suggests this robustness may extend to interacting systems, potentially enabling many-body localized phases with topologically protected edge modes [75]. Neutral atoms offer an ideal platform to study these phenomena, by combining the observation of edge modes [29] with bulk expansion in homogeneous lattices [76, 77] and tunable interactions. Intriguingly, numerical studies suggest that the modulation scheme employed in our current work indeed supports the existence of an AFAI phase, as schematically illustrated in Fig. 4a. Adding an additional perturbation in the form of a homogeneous artificial magnetic field may enable experimental studies of a quantized bulk response [78] and open the door to experimental studies of the topological magnetoelectric effect of 3D topological insulators [79].

ACKNOWLEDGMENTS

Acknowledgments: We thank W. Hofstetter and his team for fruitful discussions. This work was funded by the Deutsche Forschungsgemeinschaft (DFG, German Research Foundation) via Research Unit FOR 2414 under project number 277974659. The work was further supported under Germany's Excellence Strategy – EXC-2111-3908148, by the Alfred Krupp von Bohlen und Halbach foundation and under Horizon Europe programme HORIZON-CL4-2022-QUANTUM-02-SGA via the project 101113690 (PASQuanS2.1).

Materials and Correspondence: Correspondence and requests for materials should be addressed to monika.aidelsburger@mpq.mpg.de

-
- [1] X.-L. Qi and S.-C. Zhang, Topological insulators and superconductors, *Rev. Mod. Phys.* **83**, 1057 (2011).
 - [2] X.-G. Wen, Colloquium: Zoo of quantum-topological phases of matter, *Rev. Mod. Phys.* **89**, 041004 (2017).
 - [3] K. von Klitzing, The quantized Hall effect, *Rev. Mod.*

Phys. **58**, 519 (1986).

- [4] H. L. Stormer, D. C. Tsui, and A. C. Gossard, The fractional quantum Hall effect, *Rev. Mod. Phys.* **71**, S298 (1999).
- [5] M. Aidelsburger, S. Nascimbène, and N. Goldman, Ar-

- tificial gauge fields in materials and engineered systems, *C. R. Phys.* **19**, 394 (2018).
- [6] N. R. Cooper, J. Dalibard, and I. B. Spielman, Topological bands for ultracold atoms, *Rev. Mod. Phys.* **91**, 015005 (2019).
 - [7] C. Gross and W. S. Bakr, Quantum gas microscopy for single atom and spin detection, *Nature Phys.* **17**, 1316 (2021).
 - [8] M. Bukov, L. D'Alessio, and A. Polkovnikov, Universal high-frequency behavior of periodically driven systems: from dynamical stabilization to Floquet engineering, *Advances in Physics* **64**, 139 (2015).
 - [9] A. Eckardt, Colloquium: Atomic quantum gases in periodically driven optical lattices, *Rev. Mod. Phys.* **89**, 011004 (2017).
 - [10] C. Weitenberg and J. Simonet, Tailoring quantum gases by Floquet engineering, *Nature Phys.* **17**, 1342 (2021).
 - [11] A. Celi, P. Massignan, J. Ruseckas, N. Goldman, I. B. Spielman, G. Juzeliūnas, and M. Lewenstein, Synthetic Gauge Fields in Synthetic Dimensions, *Phys. Rev. Lett.* **112**, 043001 (2014).
 - [12] M. Mancini, G. Pagano, G. Cappellini, L. Livi, M. Rider, J. Catani, C. Sias, P. Zoller, M. Inguscio, M. Dalmonte, and L. Fallani, Observation of chiral edge states with neutral fermions in synthetic Hall ribbons, *Science* **349**, 1510 (2015).
 - [13] L. F. Livi, G. Cappellini, M. Diem, L. Franchi, C. Clivati, M. Frittelli, F. Levi, D. Calonico, J. Catani, M. Inguscio, and L. Fallani, Synthetic Dimensions and Spin-Orbit Coupling with an Optical Clock Transition, *Phys. Rev. Lett.* **117**, 220401 (2016).
 - [14] S. Kolkowitz, S. L. Bromley, T. Bothwell, M. L. Wall, G. E. Marti, A. P. Koller, X. Zhang, A. M. Rey, and J. Ye, Spin-orbit-coupled fermions in an optical lattice clock, *Nature* **542**, 66 (2017).
 - [15] M. Aidelsburger, M. Atala, M. Lohse, J. T. Barreiro, B. Paredes, and I. Bloch, Realization of the Hofstadter Hamiltonian with Ultracold Atoms in Optical Lattices, *Phys. Rev. Lett.* **111**, 185301 (2013).
 - [16] H. Miyake, G. A. Siviloglou, C. J. Kennedy, W. C. Burton, and W. Ketterle, Realizing the Harper Hamiltonian with Laser-Assisted Tunneling in Optical Lattices, *Phys. Rev. Lett.* **111**, 185302 (2013).
 - [17] M. E. Tai, A. Lukin, M. Rispoli, R. Schittko, T. Menke, Dan Borgnia, P. M. Preiss, F. Grusdt, A. M. Kaufman, and M. Greiner, Microscopy of the interacting Harper-Hofstadter model in the two-body limit, *Nature* **546**, 519 (2017).
 - [18] G. Jotzu, M. Messer, R. Desbuquois, M. Lebrat, T. Uehlinger, D. Greif, and T. Esslinger, Experimental realization of the topological Haldane model with ultracold fermions, *Nature* **515**, 237 (2014).
 - [19] M. Tarnowski, F. N. Ünal, N. Fläschner, B. S. Rem, A. Eckardt, K. Sengstock, and C. Weitenberg, Measuring topology from dynamics by obtaining the Chern number from a linking number, *Nature Commun.* **10**, 1 (2019).
 - [20] K. Wintersperger, C. Braun, F. N. Ünal, A. Eckardt, M. D. Liberto, N. Goldman, I. Bloch, and M. Aidelsburger, Realization of an anomalous floquet topological system with ultracold atoms, *Nature Phys.* **16**, 1058 (2020).
 - [21] J. Léonard, S. Kim, J. Kwan, P. Segura, F. Grusdt, C. Repellin, N. Goldman, and M. Greiner, Realization of a fractional quantum Hall state with ultracold atoms, *Nature* **619**, 495 (2023).
 - [22] T.-W. Zhou, G. Cappellini, D. Tusi, L. Franchi, J. Paravicini, C. Repellin, S. Greschner, M. Inguscio, T. Giamarchi, M. Filippone, J. Catani, and L. Fallani, Observation of universal Hall response in strongly interacting Fermions, *Science* **381**, 427 (2023).
 - [23] A. Impertro, S. Huh, S. Karch, J. F. Wienand, I. Bloch, and M. Aidelsburger, Strongly interacting Meissner phases in large bosonic flux ladders, *Nature Physics* **21**, 895 (2025).
 - [24] M. Atala, M. Aidelsburger, J. T. Barreiro, D. Abanin, T. Kitagawa, E. Demler, and I. Bloch, Direct measurement of the Zak phase in topological Bloch bands, *Nature Phys.* **9**, 795 (2013).
 - [25] L. Duca, T. Li, M. Reitter, I. Bloch, M. Schleier-Smith, and U. Schneider, An Aharonov-Bohm interferometer for determining Bloch band topology, *Science* **347**, 288 (2015).
 - [26] M. Aidelsburger, M. Lohse, C. Schweizer, M. Atala, J. T. Barreiro, S. Nascimbène, N. R. Cooper, I. Bloch, and N. Goldman, Measuring the Chern number of Hofstadter bands with ultracold bosonic atoms, *Nature Phys.* **11**, 162 (2015).
 - [27] N. Fläschner, B. S. Rem, M. Tarnowski, D. Vogel, D.-S. Lühmann, K. Sengstock, and C. Weitenberg, Experimental reconstruction of the Berry curvature in a Floquet Bloch band, *Science* **352**, 1091 (2016).
 - [28] L. Asteria, D. Thanh Tran, T. Ozawa, M. Tarnowski, B. S. Rem, N. Fläschner, K. Sengstock, N. Goldman, and C. Weitenberg, Measuring quantized circular dichroism in ultracold topological matter, *Nature Phys.* **15**, 449 (2019).
 - [29] C. Braun, R. Saint-Jalm, A. Hesse, J. Arceri, I. Bloch, and M. Aidelsburger, Real-space detection and manipulation of topological edge modes with ultracold atoms, *Nature Phys.* **20**, 1306 (2024).
 - [30] P. Titum, N. H. Lindner, M. C. Rechtsman, and G. Refael, Disorder-Induced Floquet Topological Insulators, *Phys. Rev. Lett.* **114**, 056801 (2015).
 - [31] P. Titum, E. Berg, M. S. Rudner, G. Refael, and N. H. Lindner, Anomalous Floquet-Anderson Insulator as a nonadiabatic quantized charge pump, *Phys. Rev. X* **6**, 021013 (2016).
 - [32] J.-H. Zheng, A. Dutta, M. Aidelsburger, and W. Hofstadter, Floquet topological phase transitions induced by uncorrelated or correlated disorder, *Phys. Rev. B* **109**, 184201 (2024).
 - [33] A. Dutta, E. Sen, J.-H. Zheng, M. Aidelsburger, and W. Hofstadter, Anomalous Floquet Anderson insulator in a continuously driven optical lattice, *Phys. Rev. B* **109**, L121114 (2024).
 - [34] R. Citro and M. Aidelsburger, Thouless pumping and topology, *Nat. Rev. Phys.* **5**, 87 (2023).
 - [35] Q. Niu and D. J. Thouless, Quantised adiabatic charge transport in the presence of substrate disorder and many-body interaction, *J. Phys. A: Math. Gen.* **17**, 2453 (1984).
 - [36] A. Cerjan, M. Wang, S. Huang, K. P. Chen, and M. C. Rechtsman, Thouless pumping in disordered photonic systems, *Light. Sci. Appl.* **9**, 178 (2020).
 - [37] S. Nakajima, N. Takei, K. Sakuma, Y. Kuno, P. Marra, and Y. Takahashi, Competition and interplay between topology and quasi-periodic disorder in Thouless pumping of ultracold atoms, *Nature Phys.* **17**, 844 (2021).

- [38] Y. Liu, Y.-R. Zhang, Y.-H. Shi, T. Liu, C. Lu, Y.-Y. Wang, H. Li, T.-M. Li, C.-L. Deng, S.-Y. Zhou, T. Liu, J.-C. Zhang, G.-H. Liang, Z.-Y. Mei, W.-G. Ma, H.-T. Liu, Z.-H. Liu, C.-T. Chen, K. Huang, X. Song, S. P. Zhao, Y. Tian, Z. Xiang, D. Zheng, F. Nori, K. Xu, and H. Fan, Interplay between disorder and topology in Thouless pumping on a superconducting quantum processor, *Nature Commun.* **16**, 108 (2025).
- [39] I. H. Grinberg, M. Lin, C. Harris, W. A. Benalcazar, C. W. Peterson, T. L. Hughes, and G. Bahl, Robust temporal pumping in a magneto-mechanical topological insulator, *Nature Commun.* **11**, 974 (2020).
- [40] E. J. Meier, F. A. An, A. Dauphin, M. Maffei, P. Massignan, T. L. Hughes, and B. Gadway, Observation of the topological Anderson insulator in disordered atomic wires, *Science* **362**, 929 (2018).
- [41] S. Stützer, Y. Plotnik, Y. Lumer, P. Titum, N. H. Lindner, M. Segev, M. C. Rechtsman, and A. Szameit, Photonic topological Anderson insulators, *Nature* **560**, 461 (2018).
- [42] G.-G. Liu, Y. Yang, X. Ren, H. Xue, X. Lin, Y.-H. Hu, H.-x. Sun, B. Peng, P. Zhou, Y. Chong, and B. Zhang, Topological Anderson Insulator in Disordered Photonic Crystals, *Phys. Rev. Lett.* **125**, 133603 (2020).
- [43] X.-D. Chen, Z.-X. Gao, X. Cui, H.-C. Mo, W.-J. Chen, R.-Y. Zhang, C. T. Chan, and J.-W. Dong, Realization of Time-Reversal Invariant Photonic Topological Anderson Insulators, *Phys. Rev. Lett.* **133**, 133802 (2024).
- [44] B. I. Halperin, Quantized Hall conductance, current-carrying edge states, and the existence of extended states in a two-dimensional disordered potential, *Phys. Rev. B* **25**, 2185 (1982).
- [45] Y. Hatsugai, Chern number and edge states in the integer quantum Hall effect, *Phys. Rev. Lett.* **71**, 3697 (1993).
- [46] P. Bouyer, Quantum gases and optical speckle: a new tool to simulate disordered quantum systems, *Rep. Prog. Phys.* **73**, 062401 (2010).
- [47] J. W. Goodman, *Speckle Phenomena in Optics: Theory and Applications* (SPIE Press, 2020).
- [48] See Supplemental Material, which includes Refs [80–82], for additional information on the experimental sequence and the disorder setup, calibration and alignment procedures, data analysis, error estimates and numerical simulations of the Bott index and edge-mode propagation.
- [49] D. Clément, A. F. Varón, M. Hugbart, J. A. Retter, P. Bouyer, L. Sanchez-Palencia, D. M. Gangardt, G. V. Shlyapnikov, and A. Aspect, Suppression of Transport of an Interacting Elongated Bose-Einstein Condensate in a Random Potential, *Phys. Rev. Lett.* **95**, 170409 (2005).
- [50] V. V. Volchkov, M. Pasek, V. Denechaud, M. Mukhtar, A. Aspect, D. Delande, and V. Josse, Measurement of Spectral Functions of Ultracold Atoms in Disordered Potentials, *Phys. Rev. Lett.* **120**, 060404 (2018).
- [51] A. Rubio-Abadal, J.-y. Choi, J. Zeiher, S. Hollerith, J. Rui, I. Bloch, and C. Gross, Many-Body Delocalization in the Presence of a Quantum Bath, *Phys. Rev. X* **9**, 041014 (2019).
- [52] T. Kitagawa, E. Berg, M. Rudner, and E. Demler, Topological characterization of periodically driven quantum systems, *Phys. Rev. B* **82**, 235114 (2010).
- [53] M. S. Rudner, N. H. Lindner, E. Berg, and M. Levin, Anomalous Edge States and the Bulk-Edge Correspondence for Periodically Driven Two-Dimensional Systems, *Phys. Rev. X* **3**, 031005 (2013).
- [54] F. Nathan and M. S. Rudner, Topological singularities and the general classification of Floquet-Bloch systems, *New J. Phys.* **17**, 125014 (2015).
- [55] J. Billy, V. Josse, Z. Zuo, A. Bernard, B. Hambrecht, P. Lugan, D. Clément, L. Sanchez-Palencia, P. Bouyer, and A. Aspect, Direct observation of Anderson localization of matter waves in a controlled disorder, *Nature* **453**, 891 (2008).
- [56] G. Roati, C. D’Errico, L. Fallani, M. Fattori, C. Fort, M. Zaccanti, G. Modugno, M. Modugno, and M. Inguscio, Anderson localization of a non-interacting Bose-Einstein condensate, *Nature* **453**, 895 (2008).
- [57] S. S. Kondov, W. R. McGehee, J. J. Zirbel, and B. DeMarco, Three-Dimensional Anderson Localization of Ultracold Matter, *Science* **334**, 66 (2011).
- [58] F. Jendrzejewski, A. Bernard, K. Müller, P. Cheinet, V. Josse, M. Piraud, L. Pezzé, L. Sanchez-Palencia, A. Aspect, and P. Bouyer, Three-dimensional localization of ultracold atoms in an optical disordered potential, *Nature Phys.* **8**, 398 (2012).
- [59] G. Semeghini, M. Landini, P. Castilho, S. Roy, G. Spagnolli, A. Trenkwalder, M. Fattori, M. Inguscio, and G. Modugno, Measurement of the mobility edge for 3D Anderson localization, *Nature Phys.* **11**, 554 (2015).
- [60] B. Lecoutre, Y. Guo, X. Yu, M. Niranjan, M. Mukhtar, V. V. Volchkov, A. Aspect, and V. Josse, Bichromatic state-dependent disordered potential for Anderson localization of ultracold atoms, *Eur. Phys. J. D* **76**, 218 (2022).
- [61] J. Guglielmon and M. C. Rechtsman, Broadband Topological Slow Light through Higher Momentum-Space Winding, *Phys. Rev. Lett.* **122**, 153904 (2019).
- [62] J. F. Karcher, S. Gopalakrishnan, and M. C. Rechtsman, Stability of topologically protected slow light against disorder, *Phys. Rev. A* **109**, 063507 (2024).
- [63] T. D. Stanescu, V. Galitski, and S. Das Sarma, Topological states in two-dimensional optical lattices, *Phys. Rev. A* **82**, 013608 (2010).
- [64] M. Buchhold, D. Cocks, and W. Hofstetter, Effects of smooth boundaries on topological edge modes in optical lattices, *Phys. Rev. A* **85**, 063614 (2012).
- [65] N. Goldman, J. Dalibard, A. Dauphin, F. Gerbier, M. Lewenstein, P. Zoller, and I. B. Spielman, Direct imaging of topological edge states in cold-atom systems, *PNAS* **11**, 6736 (2013).
- [66] T. A. Loring and M. B. Hastings, Disordered topological insulators via C^* -algebras, *EPL* **92**, 67004 (2011).
- [67] D. Toniolo, On the Bott index of unitary matrices on a finite torus, *Lett. Math. Phys.* **112** (2022).
- [68] A. Zenesini, D. Ciampini, O. Morsch, and E. Arimondo, Observation of Stückelberg oscillations in accelerated optical lattices, *Phys. Rev. A* **82**, 065601 (2010).
- [69] S. Kling, T. Salger, C. Grossert, and M. Weitz, Atomic Bloch-Zener Oscillations and Stückelberg Interferometry in Optical Lattices, *Phys. Rev. Lett.* **105**, 215301 (2010).
- [70] A. Kundu, M. Rudner, E. Berg, and N. H. Lindner, Quantized large-bias current in the anomalous Floquet-Anderson insulator, *Phys. Rev. B* **101**, 041403 (2020).
- [71] B. Wang, M. Aidelsburger, J. Dalibard, A. Eckardt, and N. Goldman, Cold-atom elevator: From edge-state injection to the preparation of fractional chern insulators, *Phys. Rev. Lett.* **132**, 163402 (2024).
- [72] A. Impertro, S. Karch, J. F. Wienand, S. Huh, C. Schweizer, I. Bloch, and M. Aidelsburger, Local Read-

- out and Control of Current and Kinetic Energy Operators in Optical Lattices, *Phys. Rev. Lett.* **133**, 063401 (2024).
- [73] C. I. Timms, L. M. Sieberer, and M. H. Kolodrubetz, Quantized Floquet Topology with Temporal Noise, *Phys. Rev. Lett.* **127**, 270601 (2021).
 - [74] P.-P. Zheng, C. I. Timms, and M. H. Kolodrubetz, Anomalous Floquet-Anderson insulator with quasiperiodic temporal noise, *Phys. Rev. B* **108**, 094207 (2023).
 - [75] F. Nathan, D. Abanin, E. Berg, N. H. Lindner, and M. S. Rudner, Anomalous Floquet insulators, *Phys. Rev. B* **99**, 195133 (2019).
 - [76] U. Schneider, L. Hackermüller, J. P. Ronzheimer, S. Will, S. Braun, T. Best, I. Bloch, E. Demler, S. Mandt, D. Rasch, and A. Rosch, Fermionic transport and out-of-equilibrium dynamics in a homogeneous Hubbard model with ultracold atoms, *Nature Phys.* **8**, 213 (2012).
 - [77] J. P. Ronzheimer, M. Schreiber, S. Braun, S. S. Hodgman, S. Langer, I. P. McCulloch, F. Heidrich-Meisner, I. Bloch, and U. Schneider, Expansion Dynamics of Interacting Bosons in Homogeneous Lattices in One and Two Dimensions, *Phys. Rev. Lett.* **110**, 205301 (2013).
 - [78] F. Nathan, M. S. Rudner, N. H. Lindner, E. Berg, and G. Refael, Quantized Magnetization Density in Periodically Driven Systems, *Phys. Rev. Lett.* **119**, 186801 (2017).
 - [79] L. P. Gavensky, N. Goldman, and G. Usaj, Quantized Chern-Simons Axion Coupling in Anomalous Floquet Systems, [arXiv:2506.20719](https://arxiv.org/abs/2506.20719) (2025).
 - [80] J. H. Huckans, I. B. Spielman, B. L. Tolra, W. D. Phillips, and J. V. Porto, Quantum and classical dynamics of a Bose-Einstein condensate in a large-period optical lattice, *Phys. Rev. A* **80** (2009).
 - [81] B. Gadway, D. Pertot, R. Reimann, M. G. Cohen, and D. Schneble, Analysis of Kapitza-Dirac diffraction patterns beyond the Raman-Nath regime, *Optics Express* **17**, 19173 (2009).
 - [82] G. Reinaudi, T. Lahaye, Z. Wang, and D. Guéry-Odelin, Strong saturation absorption imaging of dense clouds of ultracold atoms, *Opt. Lett.* **32**, 3143 (2007).

SUPPLEMENTAL MATERIAL

S.I Experimental sequence	10
S.II Disorder potential	10
S.III Disorder calibration	11
S.IV Tweezer alignment routine	13
S.V Measuring the phase transition for zero disorder	13
S.VI Data evaluation	14
S.VII Bott index evaluation	14
S.VIII Numerical edge state propagation	15

S.I. EXPERIMENTAL SEQUENCE

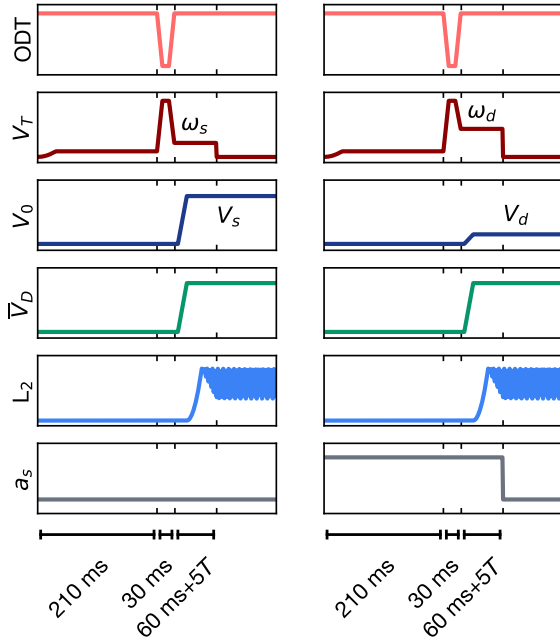


Figure S1. **Experimental sequence.** Illustration of the experimental sequence. The differences for the two different initial-state-preparations are illustrated (left: shallow, right: deep). ODT denotes the intensity of the crossed optical dipole trap, V_T the intensity of the optical tweezer beam, V_0 the intensity of the hard-wall potential, \bar{V}_D the intensity of the disorder potential, L_2 is the intensity of one of the three lattice beams, and a is the scattering length.

To optimize the signal when probing the edge states in both the Haldane as well as in the anomalous regime, it is crucial to optimize the number of atoms transferred

into the edge state, as well as the edge state velocity. The differences in the preparation protocol for the edge mode in the anomalous (left) and in the Haldane (right) regime are illustrated in Fig. S1. In both cases, we load the atoms from a BEC of ^{39}K into the optical tweezer within 210 ms. Subsequently, within 30 ms the tweezer power is briefly increased, while the dipole trap power is reduced, such that atoms not trapped in the tweezer are expelled. Afterwards, the tweezer power is ramped down to its final value, i.e., to a radial confinement frequency $\omega_s/(2\pi) = 1.3(1)$ kHz or $\omega_d/(2\pi) = 2.0(1)$ kHz depending on the measurement, as discussed in the main text. From now on the tweezer potential is kept constant, while the other potentials are being ramped up.

First, we ramp up both the potential step used to generate the topological interface V_0 generated by a DMD simultaneously with the disorder potential \bar{V}_D within 30 ms. As the edge state velocity depends on the height of the topological interface, we ramp it to $V_d/h = 2.8$ kHz for the Haldane regime, and to $V_s/h = 13.2$ kHz for the anomalous regime, to maximize the edge state velocity and hence the signal-to-noise [29].

Subsequently, we ramp up the optical lattice to a lattice depth of $5.9E_R$ within 30 ms. Finally, we ramp the amplitude of the lattice modulation m to its final value within five modulation cycles. As a last step, we reduce the scattering length one ms before releasing the atoms from $13a_0$ to $6a_0$ when preparing the edge state in the Haldane regime, while it was constant at $6a_0$ for the preparation scheme in the anomalous regime. Keeping the scattering length at a higher value reduces atom loss due to the stronger confinement at a trap frequency of 2 kHz. To initiate the dynamics in the periodically-modulated lattice, we abruptly switch off the tweezer potential.

S.II. DISORDER POTENTIAL

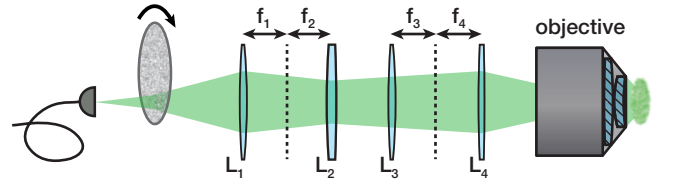


Figure S2. **Setup for generating the speckle potential:** A speckle potential is generated by illuminating a diffuser, and optically Fourier transforming it. Afterwards, it is demagnified by two telescopes, formed by L_2 and L_3 as well as L_4 and the objective. Vertical dashed lines indicate the location of planes conjugate to the atoms.

The disorder potential is generated by projecting the Fourier plane of a diffuser onto the atoms, yielding a speckle pattern. For this, a holographic diffuser (Edmund

Optics #35-693, with a 2° diffusing angle) is illuminated at 532 nm with the uncollimated output of an optical fiber (NKT Photonics aeroGUIDE POWER, seeded by a Lighthouse Sprout-G-15W). The diffuser is mounted in a rotation mount, such that it is illuminated off-center. Rotating the mount allows to illuminate different phase patches on the diffuser, yielding different speckle patterns.

The image on the diffuser is Fourier-transformed by L1 ($f_1 = 100$ mm), and subsequently demagnified by a factor 45 by two telescopes ($f_2 = 150$ mm, $f_3 = 100$ mm, and $f_4 = 750$ mm together with our objective with focal length $f_{\text{obj}} = 25$ mm).

From images recorded in an intermediary image plane we extract a radial correlation length of $7.9 \mu\text{m}$, which after demagnification by a factor 30 is consistent with a numerically simulated correlation length of 296 nm in the atomic plane. For the numerical estimate, we initialize the beam in the back focal plane of the objective and propagate it to the entrance pupil using a Fresnel propagation kernel. We then clip the wings of the beam according to the aperture of the objective and Fourier transform it to obtain the field distribution in the atomic plane. The simulation takes two input parameters, the envelope and the correlation length in the back focal plane, which determine the properties of the speckle. The envelope was directly measured in the back focal plane, and is compatible with the correlation length of the images obtained in the intermediary image plane. The correlation length of the beam in the back focal plane is inferred from the envelope on the images taken in the intermediary image plane. We attribute an error of ± 2 mm to the measurement of the beam waist in the back focal plane, which results in a correlation length $\sigma_r = 296_{-7}^{+11}$ nm.

To estimate the correlation length of the pattern along the optical axis of the objective, we determine an effective numerical aperture NA_{eff} of our objective that corresponds to the computed correlation length $\sigma_r = 296$ nm using the standard relation [47]

$$\sigma_r = \frac{\lambda}{4 \cdot \text{NA}_{\text{eff}}}. \quad (\text{S.1})$$

Using the relation between the radial and the axial correlation length via the effective numerical aperture

$$\sigma_z \approx 0.89 \frac{\lambda}{\text{NA}_{\text{eff}}^2}, \quad (\text{S.2})$$

we obtain $\sigma_z = 2.4 \mu\text{m}$.

S.III. DISORDER CALIBRATION

To determine the strength of the disorder in our experiment, we devised a calibration scheme for the speckle potential that directly measures the average potential

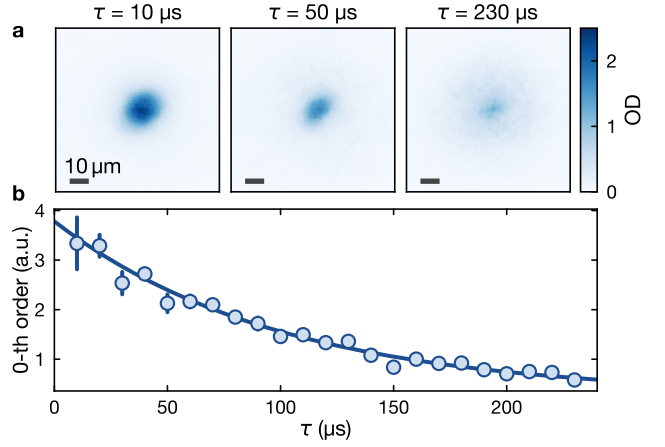


Figure S3. **Speckle diffraction of the BEC.** **a** Absorption images of the atoms after interaction with a speckle potential with strength $\bar{V}_D/h = 2.9$ kHz for different pulse durations τ . The images are taken after 8 ms of expansion in the dipole trap, and averaged over 21 disorder realizations. The scale bar in the bottom left corner indicates $10 \mu\text{m}$. **b** Zeroth order contribution to the atomic density as a function of the speckle pulse duration τ . Each data point is the average over 21 disorder realizations. The error bars on the data points have been extracted via bootstrapping. The timescale over which the zeroth order decays is determined through an exponential fit with offset (solid line).

strength \bar{V}_D in the atomic plane, which is crucial for a quantitative analysis of the disorder-driven shift of the topological phase transition. We start out with a BEC consisting of $\approx 2 \times 10^5$ atoms of ^{39}K at scattering length $6a_0$ in a crossed optical dipole trap with a horizontal trap frequency on the order of $\omega_r/(2\pi) = 25$ Hz, and a vertical trap frequency of $\omega_z/(2\pi) = 0.33(3)$ kHz. In analogy to Kapitza-Dirac diffraction of a BEC in a pulsed optical lattice [80, 81], we abruptly switch on the speckle potential for a short interaction time τ between $10 \mu\text{s}$ and $230 \mu\text{s}$. Subsequently, the atoms are held in the crossed dipole trap for a time of 8 ms. One can now observe an exponential decay in atom number from the unscattered atoms as a function of pulse length, which we quantify by performing a two-component fit as described below. By comparing this with the results obtained by numerically simulating a single-particle wavefunction evolving under the pulsed potential, the average potential depth of the speckle is inferred.

During the pulse, the atoms are coupled to different momenta according to the Fourier transform \tilde{V} of the disorder potential

$$\langle \vec{k} | V | \vec{k}' \rangle = \int d\vec{x} V(\vec{x}) e^{-i(\vec{k}-\vec{k}')\vec{x}} = \tilde{V}(\Delta\vec{k}). \quad (\text{S.3})$$

For short pulses ($\tau\bar{V}_D \sim 1$), the final wavefunction in momentum-space is bimodal, which is apparent in the time-of-flight absorption images that are shown in the top panel of Fig. S3. The strong, central peak can be at-

tributed to a remnant, unscattered fraction of the initial wavefunction, which we refer to as zeroth order contribution. It is surrounded by a broad distribution of scattered atoms that originates from the interaction with the speckle potential. In the bottom panel of Fig. S3, we plot the evolution of the zeroth order contribution as a function of pulse duration extracted by performing a two-component fit of a broad Gaussian for the scattered, and a narrower Thomas-Fermi function for the unscattered atoms. It decays exponentially with the duration of the pulse, where the decay rate Γ depends on the average potential strength.

To identify the scaling between the decay rate and the disorder strength, we use exact diagonalization to simulate the dynamics of a single-particle wavefunction evolving in the presence of a speckle potential in two dimensions. For the computation, the initial wavefunction in the form of a Thomas-Fermi profile is expanded in a 2D Fourier series that is truncated for large wavevectors. The resolution in k -space is adjusted to the radius of the BEC $\Delta k/(2\pi) = 1/2r_{\text{BEC}}$ and the cutoff is justified by the suppression of couplings to higher momentum states through the kinetic energy offset. The final grid size of the expansion in k -space is 143×143 , such that the dimension of the Hilbert space that is diagonalized is 20449. The unscattered fraction after time-evolution is extracted via the parameter A of a two-component fit to the modulus square of the resulting wavefunction

$$|\psi(\vec{k}, \tau)|^2 = A|\psi(\vec{k}, 0)|^2 + B e^{-k^2/2\sigma_k^2}, \quad (\text{S.4})$$

with 3 independent fitting parameters A, B and σ_k . After variation of the average speckle strength, we extract the curve $\Gamma(\bar{V}_D) = \bar{V}_D^{a+1} \cdot (b \cdot \bar{V}_D^a + c)^{-1}$ by fitting the three free parameters a, b, c to the simulated decay rates.

Experimentally, the power of the speckle beam is stabilized onto a photodiode located immediately next to the fiber output on the experimental table. The average intensity and thus also disorder strength in the atomic plane is directly proportional to the photodiode voltage according to $\bar{V}_D/h = \alpha \cdot U_{\text{PD}}$, with U_{PD} being the photodiode voltage. To find α , we perform a single parameter fit of the experimental data to the numerically calculated calibration curve (Fig. S4). This procedure corresponds to a rescaling of the horizontal axis of the plot, while leaving the vertical axis with the measured decay rates unchanged. For the specific case of our optical setup, we obtain $\alpha = 9.24 \text{ kHz V}^{-1}$.

To estimate the error, we consider multiple factors: First, we notice that the decay of the zeroth-order in the simulation slows down and is no longer captured well by a single exponential. Therefore, we extract a systematic error on the determination of the decay constant by varying the time window considered for the exponential fit. Starting from a fit that captures the initial, fast decay ($\tau \bar{V}_D \in [0.2, 0.6]$ depending on the disorder strength), we increase the window size until the full decay is taken into account for the fit. In this manner, we find the largest

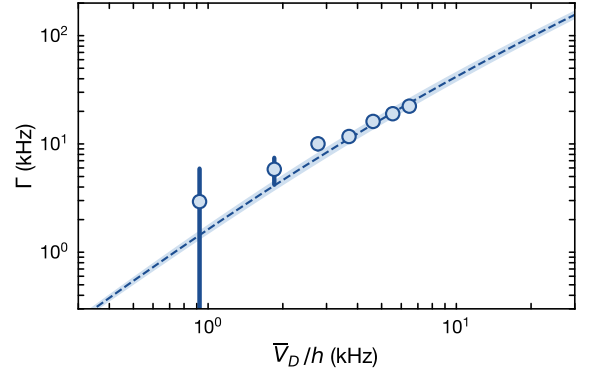


Figure S4. **Experimental disorder calibration.** The proportionality constant α connecting photodiode voltage to disorder strength in the atomic plane is obtained by fitting the experimentally measured decay rates (blue dots) to the numerical obtained function $\Gamma(\bar{V}_D)$ (dashed line). The shaded region around $\Gamma(\bar{V}_D)$ marks the systematic uncertainty in the determination of the three parameters, determined by varying the window length on which the numerically simulated decay rates are fitted. Each experimental data point is the fitted decay constant from a measurement as illustrated in Fig. S3b, consisting of 23 data points, each being the average over 21 different disorder realizations. The error bars are the fit error of the decay rate Γ .

and smallest possible decay constants for every disorder strength. We then fit the experimental data to these limits to estimate the error $\Delta_{\text{decay}} = \begin{pmatrix} +0.64 \\ -0.51 \end{pmatrix} \text{ kHz V}^{-1}$. The estimate of the correlation length of the speckle pattern is based on the waist of the speckle beam in the back focal plane of the objective and measurements of the correlation length in the intermediary image plane, as described in S.II. As the correlation length of the speckle pattern slightly impacts the decay rates, we perform the numerical simulations for the upper and lower estimate of the correlation lengths to extract an error on the calibration $\Delta_{\text{corr}} = \begin{pmatrix} +0.24 \\ -0.05 \end{pmatrix} \text{ kHz V}^{-1}$. Another factor influencing the decay curve is the diameter of the BEC probing the speckle pattern. We vary the size of the BEC by $\pm 2 \mu\text{m}$, and perform the calibration on the calibration curves obtained this way, yielding $\Delta_{\text{BEC}} = \pm 0.05 \text{ kHz V}^{-1}$. Finally, the enveloping of the speckle pattern in the atomic plane leads to a varying potential strength due to the movement of the atoms. We estimate this error to be $\Delta_{\text{envelope}} = \pm 0.11 \text{ kHz V}^{-1}$.

Combining these factors, we obtain the final calibration constant $\alpha = \left(9.24 \pm (0.25)_{\text{stat}} \begin{pmatrix} +0.93 \\ -0.61 \end{pmatrix}_{\text{sys}} \right) \text{ kHz V}^{-1}$. Here, Δ_{decay} , Δ_{corr} and Δ_{BEC} contribute as systematic errors to the measurement, and Δ_{envelope} together with the fit error of α onto the calibration curve (which originates from the uncertainty in estimating the unscattered atom fraction, captured via bootstrapping) contribute as statistic errors.

S.IV. TWEEZER ALIGNMENT ROUTINE

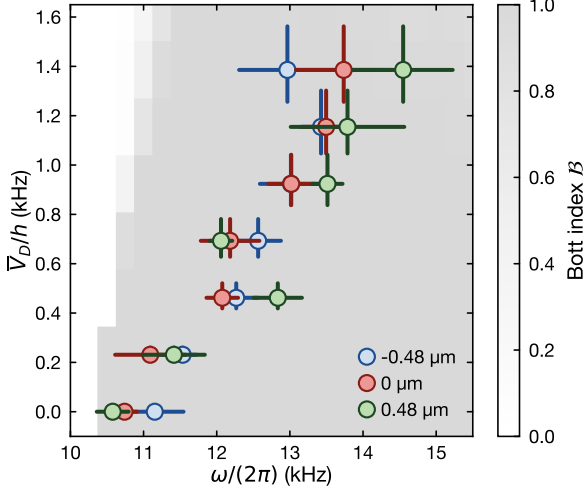


Figure S5. **Tracking the phase transition at different positions.** Location of the phase transition for varying disorder, data taken at three different locations perpendicular to the wall. Each data point is the average over 5 to 7 disorder realizations. The error bars are the fit error, analogous to Fig. 3 in the main text.

Before each experimental run, the position of the tweezer was aligned to the potential step by varying the tweezer position with respect to the step, optimizing the strength of the edge state signal. As different wall heights are required to obtain a large signal in the Haldane- and anomalous regime, the tweezer position was optimized separately to deliver a strong signal at $\omega/(2\pi) = 7$ kHz for the shallow tweezer and at $\omega/(2\pi) = 16$ kHz for the deep tweezer, as at these modulation frequencies the energy gaps are reasonably large. In the following, data was taken at the location, where the absolute value of the difference signal $|\Delta OD|$ integrated in a region close to the edge of the system was maximized. Here, for data taken with the shallow tweezer settings (ω_s, V_s) the position was chosen where the edge state signal at $\omega/(2\pi) = 7$ kHz was maximized, and respectively for the deep tweezer settings (ω_d, V_d) the position where the edge state signal at $\omega/(2\pi) = 16$ kHz was maximized.

Furthermore, data was taken for varying tweezer positions to ensure that this alignment procedure does not introduce systematic bias into the data taken. An exemplary measurement is shown in (Fig. S5), illustrating good agreement of the observed shift of the phase transition between the anomalous and Haldane regime for different positions of the tweezer perpendicular to the wall.

S.V. MEASURING THE PHASE TRANSITION FOR ZERO DISORDER

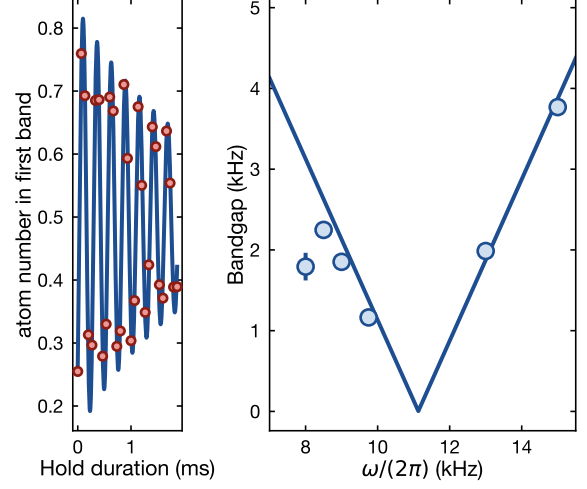


Figure S6. **Measuring the phase transition at $\bar{V}_D = 0$:** **Left:** Bandgap measured via Stückelberg interferometry at $\omega/(2\pi) = 15$ kHz. Each data point corresponds to one or two measurements. The solid line is a fit of the form $a \cdot e^{-b \cdot t} \cos(\omega t - \phi)$, with a, b, ω and ϕ being fit parameters, and $\omega/(2\pi)$ being the bandgap. **Right:** After tracking the energy gap at different modulation frequencies, we perform a fit of the form $|\omega - \omega_c|$, and obtain $\omega_c/(2\pi) = (11.13 \pm 0.08)$ kHz. Error bars are the fit error for the bandgap fit.

To benchmark the numerical simulations of the Bott index as well as the location of the phase transition extracted from the edge state evolution, we compare it to a gap-closing-measurement at $\bar{V}_D = 0$ kHz. For this, we employ Stückelberg interferometry [20, 68, 69]:

We load a bulk BEC at scattering length $6a_0$ into our optical lattice, and, while ramping up the amplitude modulation, nonadiabatically sweep the phase of two lattice beams to accelerate the atoms to the next Γ point in quasimomentum space. This nonadiabatic sweep leads to a splitting of the atom population onto the lowest two bands of our system. Subsequently, we hold the atoms at this quasimomentum for an integer number of modulation periods, and afterwards ramp lattice phase and amplitude modulation back to transfer the atoms to zero quasimomentum (at the Γ -point). Ramping the phase back nonadiabatically recombines the population in the two bands, leading to oscillations in the band population due to the acquired phase difference, as illustrated on the left in Fig. S6.

This means, that in the vicinity of a phase transition at Γ , we can observe the size of the gap reduce to zero, and increase again (right side in Fig. S6). From this we extract the phase transition for vanishing disorder $\bar{V}_D = 0$ kHz at $\omega_c/(2\pi) = 11.13(8)$ kHz, where the error bar

denotes the fit error. From a 6-band model calculation, we determine a transition frequency of 10.92 kHz.

S.VI. DATA EVALUATION

To track the movement of the edge states, we calculate the center-of-mass (COM) position of the atoms. To this end, we calculate the weighted average of the position, using the optical density extracted from absorption pictures as a weight:

$$\bar{y} = \frac{\sum_i y_i w_i}{\sum_i w_i},$$

where y_i denotes the position along the topological interface each camera pixel i corresponds to in the atomic plane, and w_i is the optical density (OD) at this pixel. The absorption pictures have been calibrated to account for saturation effects due to the non-negligible intensity of the imaging beam with respect to the saturation intensity of the atoms [82].

To track the chiral movement from this, we evaluate the difference between the position obtained for modulation with chirality $\kappa = 1$ and for modulation with chirality $\kappa = -1$ parallel to the step of the hard-wall potential.

To estimate the error in this determination, we employ bootstrapping: From the set of all absorption pictures taken with the same parameters, we choose random sets of the same length as the initial set, such that images can be selected multiple times. We perform the evaluation for 100 of such sets, and take the standard deviation in the results to be the error.

S.VII. BOTT INDEX EVALUATION

For disordered systems, lacking translational invariance, conventional topological invariants defined in terms of geometric properties of Bloch states in momentum space are no longer practical. The Bott index, introduced by Loring and Hastings [66], is a real-space topological marker that can be evaluated on a disordered lattice to quantify whether topological features prevent the existence of a set of localized wavefunctions spanning a band's eigenspace. For vanishing disorder, the Bott index of a given energy band has been shown to coincide with its Chern number in the thermodynamic limit [67]. In the following, we adopt the procedure outlined in Ref. [66] to evaluate the Bott index for the lower band of the effective Hamiltonian resulting from our periodic modulation scheme.

The sinusoidal drive of the intensity of the three laser beams interfering to form the optical honeycomb lattice results in the following time dependence for the nearest-neighbor tunneling amplitudes:

$$J_i(t) = A e^{B \cos(\omega t + \phi_i)} + C, \quad (\text{S.5})$$

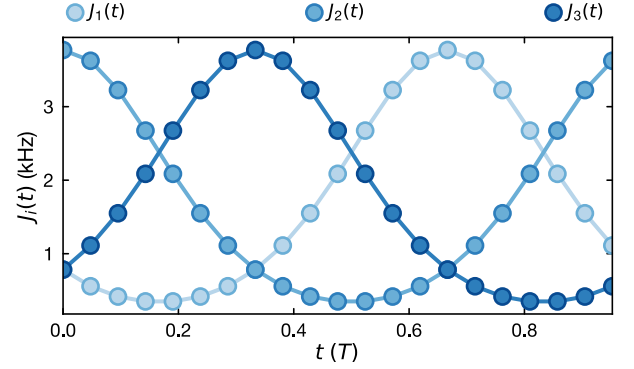


Figure S7. **Temporal discretization of nearest-neighbor tunneling modulation.** The continuous time-dependence of the tunneling rates along the three main directions of the honeycomb lattice is numerically approximated by evaluation at $N = 21$ equidistant timesteps across the modulation period.

where $\phi_i = \frac{2\pi}{3}(i-1)$, $i \in \{1, 2, 3\}$ and A , B and C are parameters that depend on the modulation amplitude m . For $m = 0.25$, as set for all experimental results discussed in the main text, $A \approx 0.220E_R$, $B \approx 0.767$ and $C \approx -0.065E_R$, with the recoil energy $E_R = \hbar^2/(2\lambda_L^2 2m_K) \approx \hbar \times 9.23$ kHz. Next-nearest neighbor tunneling amplitudes are about one order of magnitude smaller, and thereby neglected in the following. In order to evaluate the effective Hamiltonian numerically, the modulation period is discretized into N timesteps to evaluate $J_i(t_j)$ and the corresponding instantaneous Hamiltonian $\hat{H}(t_j)$ for $t_j = \frac{T}{N}j$, $j = 0, 1, \dots, N-1$. For all numerical results discussed in the main text, the number of timesteps is set to $N = 21$, resulting in the discretization of the tunneling rates along the three lattice directions shown in Fig. S7. At each timestep, $\hat{H}(t_j)$ is perturbed by an additional term \hat{V}_D , modeling on-site energy offsets $\langle x_i, y_i | \hat{V}_D | x_i, y_i \rangle$ sampled by the hexagonal lattice on a numerical speckle potential, as displayed in Fig. S8. To ensure correct ordering of eigenstates upon diagonalization, we subtract the mean of all N_s on-site energy offsets from each diagonal entry of $\hat{H}(t_j)$. Ultimately, the time-evolution operator over one modulation period reads

$$\hat{U}(T) = \prod_{j=0}^{N-1} e^{-\frac{i}{\hbar}(\hat{H}(t_{N-j-1}) + \hat{V}_D) \frac{T}{N}}, \quad (\text{S.6})$$

from which the effective Hamiltonian is readily obtained:

$$\hat{H}_{\text{eff}} = \frac{i\hbar}{T} \ln(\hat{U}(T)). \quad (\text{S.7})$$

To evaluate the Bott index for a given disorder realization, we enforce periodic boundary conditions on a rectangular system consisting of N_s lattice sites, construct \hat{H}_{eff} in real space and diagonalize it to obtain its

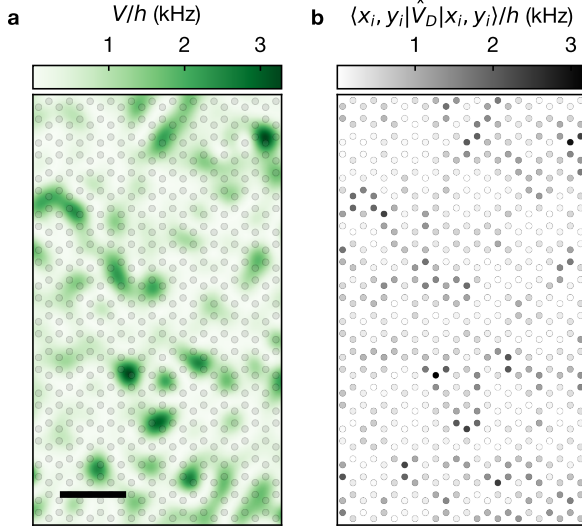


Figure S8. **Spatial sampling of on-site energy offsets from a speckle pattern.** **a**, Potential landscape from a numerical speckle pattern with $\bar{V}_D/h = 0.5$ kHz and $\sigma_r = 296$ nm over a region covered by a finite lattice consisting of $N_s = 576$ sites. The scale bar covers a distance of $5a$. **b**, Corresponding on-site energy offsets sampled by the lattice sites, contributing the same diagonal terms to the instantaneous tight-binding Hamiltonian at every timestep, as for an effectively static disorder potential.

eigenbasis $\{|\psi_n\rangle, n = 1, \dots, N_s\}$. In a second step, we construct the projector onto the lower-band eigenspace $\hat{P} = \sum_{1 \leq n \leq N_s/2} |\psi_n\rangle\langle\psi_n|$ to evaluate the following band-projected position operators:

$$\hat{G}_\alpha = \hat{P} e^{\frac{2\pi i}{L_\alpha} \hat{\alpha}} \hat{P}, \quad \alpha = x, y, \quad (\text{S.8})$$

with L_α denoting the system size in x - or y -direction. Finally, the Bott index of the lower band is given by

$$\mathcal{B} = \frac{1}{2\pi} \text{Im} \left(\text{Tr} \left(\ln \left(\hat{G}_y \hat{G}_x \hat{G}_y^\dagger \hat{G}_x^\dagger \right) \right) \right), \quad (\text{S.9})$$

where $\hat{G}_\alpha = \hat{G}_\alpha + (\hat{1} - \hat{P})$.

In the absence of disorder ($\bar{V}_D = 0$), the transition from $\mathcal{B} = 0$, corresponding to the anomalous regime, to $\mathcal{B} = 1$, corresponding to the Haldane regime, takes place at a modulation frequency $\omega/(2\pi) \approx 10.44$ kHz for $m = 0.25$, in agreement with the numerical evaluation of the corresponding Chern number in a two-band model with the same modulation scheme. Numerical estimates for transition frequencies provided by a two-band model, which do not capture higher-band corrections, systematically underestimate the transition frequency predicted by a six-band calculation, namely $\omega/(2\pi) \approx 10.92$ kHz, and the one measured experimentally, as shown in Fig. 3 in the main text and studied in detail in Ref. [20].

The number of lattice sites set for the Bott index evaluations discussed in the main text is $N_s = 576$. Figure

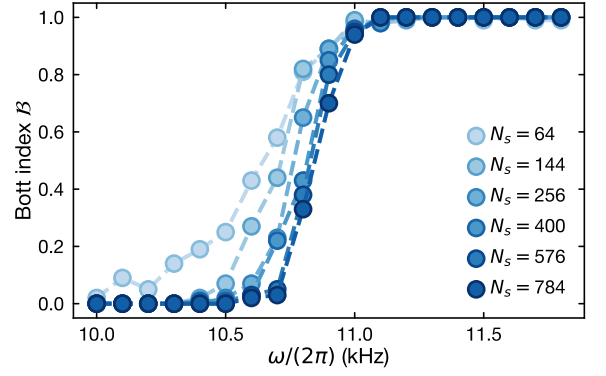


Figure S9. **Finite-size effects on average Bott index evaluation.** For increasing number of lattice size N_s , the frequency at which the transition between the anomalous ($\mathcal{B} = 0$) and the Haldane regime ($\mathcal{B} = 1$) occurs for a disorder strength of $\bar{V}_D/h = 1$ kHz converges to a fixed value for system sizes larger than $N_s = 400$. The Bott index is averaged over $N_{\text{avg}} = 100$ disorder realizations for every combination of modulation frequency and system size.

S9 shows the Bott index across the transition between the anomalous and the Haldane regime for varying system size N_s and fixed disorder strength $\bar{V}_D/h = 1$ kHz, averaged over $N_{\text{avg}} = 100$ disorder realizations. For system sizes larger than $N_s = 400$, the average Bott index converges to the thermodynamic limit, which justifies the value chosen for N_s and rules out finite-size effects.

S.VIII. NUMERICAL EDGE STATE PROPAGATION

The procedure to obtain $\hat{U}(T)$ outlined in the previous section can be employed on a lattice with closed boundary conditions to investigate the propagation dynamics of wavepackets localized to the system's numerical edges for increasing disorder strength. Repeated action of $\hat{U}(T)$ on an initial state $|\varphi_0\rangle$ provides access to the same observables probed experimentally, i.e., the COM distance. After n modulation periods, the initial state is mapped onto

$$|\varphi(t = nT)\rangle = \hat{U}(nT) |\varphi_0\rangle = \left(\hat{U}(T) \right)^n |\varphi_0\rangle. \quad (\text{S.10})$$

Depending on the overlap $|\langle\varphi_0|\psi_n\rangle|^2$ of the initial state with the eigenstates $\{|\psi_n\rangle, n = 1, \dots, N_s\}$ of the effective Hamiltonian in a given regime, the wavefunction population will propagate along the numerical boundary of the system or scatter towards its bulk. Both in the anomalous and in the Haldane regime, for a zigzag edge geometry, only the outermost lattice sites have a non-zero population for an infinitely high and steep boundary. However, as described in Ref. [29], the edge state wave functions display a uniform phase pattern in the anomalous regime and an alternating phase pattern in

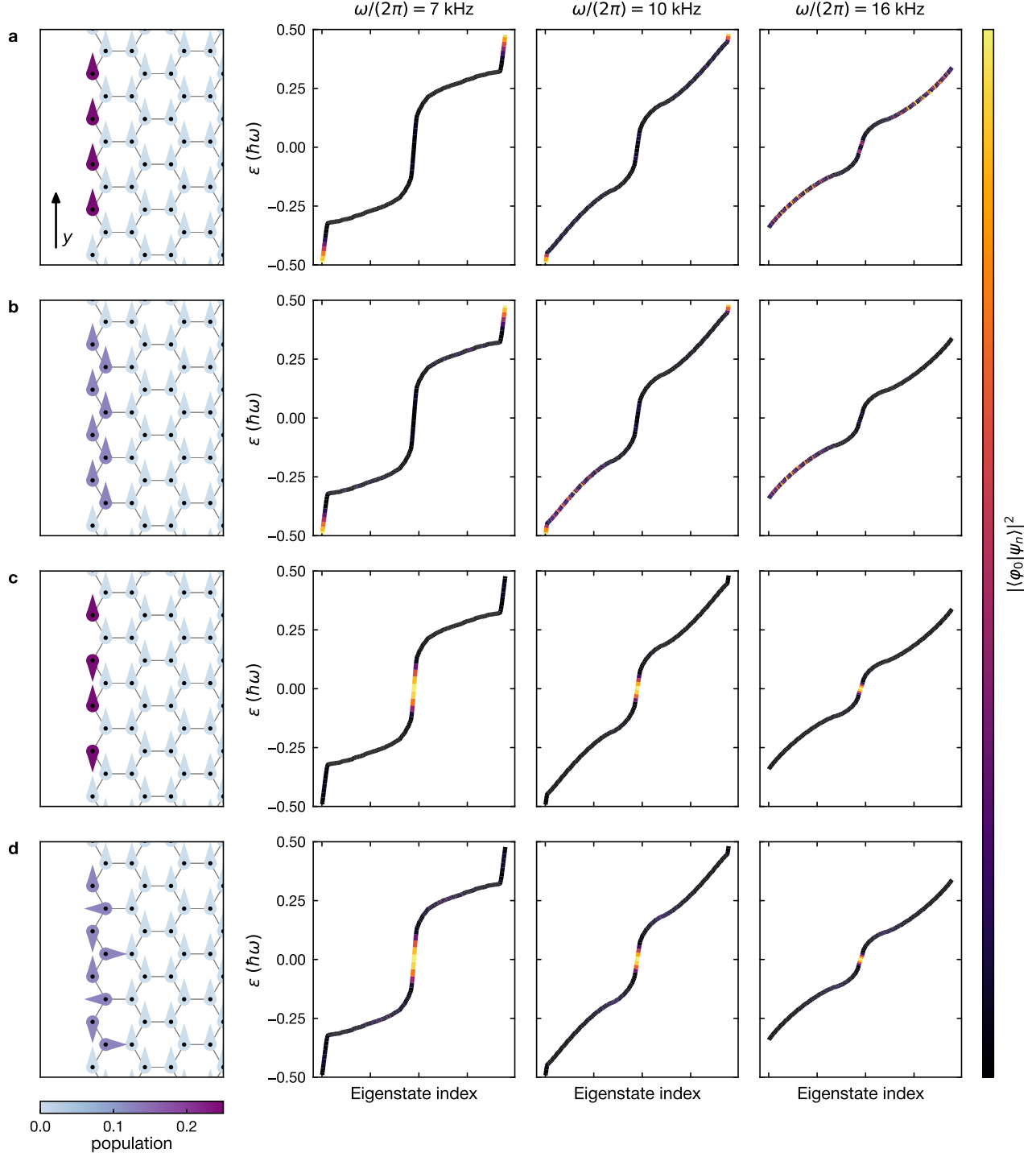


Figure S10. **Numerical edge mode preparation.** Possible choices for the initial wavefunction and corresponding overlap with the eigenstates $\{|\psi_n\rangle, n = 1, \dots, N_s\}$ of the effective Hamiltonian on a finite lattice strip deep in the anomalous regime $[\omega/(2\pi) = 7 \text{ kHz}]$, close to the transition into the Haldane regime $[\omega/(2\pi) = 10 \text{ kHz}]$ and deep in the Haldane regime $[\omega/(2\pi) = 16 \text{ kHz}]$. The little arrows indicate the site-dependent phase of the wave function. **a**, Equal distribution of the population over four next-nearest neighbors along the edge, belonging to the same sublattice, results in good overlap with the edge state in the 0-gap of the anomalous regime, but also nonvanishing overlap with the edge state in the π -gap of the Haldane regime. **b**, Populating sites on the second sublattice as well significantly reduces the overlap with the edge states in the Haldane regime. **c**, **d** The two corresponding options for $|\varphi_0\rangle$ in the Haldane regime result in similar overlaps with eigenstates at each modulation frequency considered. For the sake of visibility, the color limits of each plot displaying overlaps with eigenstates are renormalized to the corresponding maximum value.

the Haldane regime, such that $|\varphi_0\rangle$ can be initialized to have a good overlap with the edge states in the anomalous regime and vanishing overlap with the edge state in the Haldane regime, providing a numerical equivalent to the regime-sensitive state preparation achieved experimentally by varying the tweezer depth.

To closely reproduce the experimental setup, we generate lattice strips for which the system boundary in the y -direction, along which we initialize and time-propagate numerical wavepackets, displays a zigzag termination geometry. Suitable system sizes are chosen depending on the largest expansion time of interest such that edge modes do not propagate past the system's corner. This ensures that edge dynamics can be solely investigated by means of the center-of-mass in the y -direction and the time-evolution thereof. For all numerical results displayed in Fig. 2 of the main text, probing edge propagation deep in the Haldane regime up to expansion times of $80T$, numerical strips consist of $N_s = 3360$ lattice sites, with a ratio between the lengths of the system in the y - and x -direction of $L_y/L_x \approx 2.5$. On the other hand, for Fig. 3 of the main text, the fixed expansion time at which the COM distance decay is evaluated across the disorder-shifted transition amounts to $20T$, such that smaller systems with $N_s = 952$ lattice sites suffice, with a slightly larger ratio of $L_y/L_x \approx 2.8$.

Intuitively, to numerically populate edge modes in the π -gap of the anomalous regime and in the 0-gap of the Haldane regime, $|\varphi_0\rangle$ should be prepared to closely match the corresponding wavefunctions, i.e., such that only lattice sites along the boundary, belonging to the same sub-

lattice and spaced by $\sqrt{3}a$, are populated with uniform and alternating phase patterns, respectively [29], as displayed in the left panel of Fig. S10a,c. For the purposes of the numerics discussed in Fig. 3 of the main text, however, the wavefunction in Fig. S10a is seen to display a nonvanishing overlap with the edge state wavefunctions in the π -gap of a system deep in the Haldane regime, $\omega/(2\pi) = 16$ kHz (rightmost panel of Fig. S10a), resulting in a residual chiral signal in the Haldane regime. Moreover, we find that the dynamics of such an initial wavepacket is strongly influenced by the initial phase of the modulation. In contrast, we find that a slightly extended wavefunction that more closely resembles the situation realized experimentally (leftmost panel of Fig. S10b) provides a more robust observable with higher contrast. Here, also sites slightly away from the interface (on the other sublattice) are populated. This initial state displays good overlap with the edge mode of interest in the anomalous regime and vanishing overlap with the edge mode in the Haldane regime, providing a more accurate probe for the disorder-driven shift of the transition.

In the Haldane regime the transversal width of the initial state $|\varphi_0\rangle$ does not seem to play a significant role. We perform a similar comparison using the initial wavefunctions shown in the leftmost panels of Fig. S10c,d. Both yield similar results in terms of overlap with eigenstates at $\omega/(2\pi) = 16$ kHz. In principle, both initial states could be used for the numerical simulations shown in Fig. 2d. As it more closely resembles the ideal wavefunction of the 0-gap edge state, we employ the first option, distributing the population over eight sites from the same sublattice to further suppress overlap with bulk states.